New Multiply-Lensed Galaxies Identified in ACS/NIC3 Observations of Cl0024+1654 Using an Improved Mass Model

Adi Zitrin[1]⋆, Tom Broadhurst[1], Keiichi Umetsu[2,3], Dan Coe[5], Narciso Benítez[4], Begoña Ascaso[6], Larry Bradley[5], Holland Ford[5], James Jee[6], Elinor Medezinski[1], Yoel Rephaeli[1], Wei Zheng[5]

[1] *The School of Physics and Astronomy, the Raymond and Beverly Sackler Faculty of Exact Sciences, Tel Aviv University, Tel Aviv 69978, Israel*
[2] *Institute of Astronomy and Astrophysics, Academia Sinica, P. O. Box 23-141, Taipei 10617, Taiwan*
[3] *LeCosPA, National Taiwan University, Taipei 10617, Taiwan*
[4] *Instituto de Astrofísica de Andalucía (CSIC), C/Camino Bajo de Huétor, 24, Granada, 18008, Spain*
[5] *Department of Physics and Astronomy, Johns Hopkins University, 3400 North Charles Street, Baltimore, MD 21218*
[6] *Department of Physics, University of California, One Shields Avenue, Davis, CA 95616, USA*

22 September 2009

ABSTRACT

We present an improved strong-lensing analysis of Cl0024+1654 (z=0.39) using deep HST/ACS/NIC3 images, based on 33 multiply-lensed images of 11 background galaxies. These are found with a model that assumes mass approximately traces light, with a low order expansion to allow for flexibility on large scales. The model is constrained initially by the well known 5-image system (z=1.675) and refined as new multiply-lensed systems are identified using the model. Photometric redshifts of these new systems are then used to constrain better the mass profile by adopting the standard cosmological relation between redshift and lensing distance. Our model requires only 6 free parameters to describe well all positional and redshift data. The resulting inner mass profile has a slope of $d\log M/d\log r \simeq -0.55$, consistent with new weak-lensing measurements where the data overlap, at $r \simeq 200$ kpc/h_{70}. The combined profile is well fitted by a high concentration NFW mass profile, $C_{\rm vir} \sim 8.6 \pm 1.6$, similar to other well studied clusters, but larger than predicted with standard ΛCDM. A well defined radial critical curve is generated by the model and is clearly observed at $r \simeq 12''$, outlined by elongated images pointing towards the centre of mass. The relative fluxes of the multiply-lensed images are found to agree well with the modelled magnifications, providing an independent consistency check.

Key words: gravitational lensing , galaxies: clusters: individual: Cl0024+1654 , dark matter

1 INTRODUCTION

The rich cluster Cl0024+1654 is one of the most distant clusters discovered by Zwicky (1959) and displays one of the finest examples of gravitational lensing (see also Broadhurst et al. 2000). Many arcs and images of distant lensed sources are visible, among them a 5-image system of a well-resolved galaxy, which was first noted by Koo (1988, see also Smail et al. 1996). The arc mentioned by Koo (1988) was later resolved into a close triplet of arcs by Kassiola, Kovner, & Blandford (1992), while marking two additional images which were later found to be members of this system by Smail et al. (1996) and by Colley, Tyson, & Turner (1996), using HST WFPC-1 and WFPC-2 data, respectively. These arcs have been used by Colley, Tyson, & Turner (1996) to construct an image of the source, and by Tyson, Kochanski, & dell'Antonio (1998) to examine details of the mass distribution. The redshift of this system, $z = 1.675$

⋆ E-mail: adiz@wise.tau.ac.il

(Broadhurst et al. 2000), was eventually obtained from weak interstellar absorption features, permitting an accurate and fairly model-independent mass for the central area of $M(<100\text{kpc}/h)=1.11 \pm 0.03 \times 10^{14}h^{-1}M_{\odot}$ and a mass-to-light ratio of $M/L_B(<100\text{kpc}/h)=320\text{h}\pm30\text{h}(M/L_B)_{\odot}$, because of the symmetric arrangement of the images (Broadhurst et al. 2000).

Lens models for Cl0024+1654, and strong-lensing (SL) models in particular, have generally improved with higher quality imaging. Using ground based data, Kassiola, Kovner, & Blandford (1992) and Wallington, Kochanek, & Koo (1995) reproduced fits to the close triplet of arcs (A,B,C, in their notation; images 1.3, 1.4, 1.5 in Figure 7 here) but considered arc D (image 1.1 in Figure 7 here) an unlikely counter image. Subsequent HST images revealed that A,B,C and D are morphologically similar in detail (Smail et al. 1996) and that a further radially directed arc in the cluster centre, E (image 1.2 in Figure 7 here), is another complete image of the same source (Colley, Tyson, & Turner 1996, see also Broadhurst et al. 2000). A 512 parameter fit to the resolved imaging data for the arc system was presented by Tyson, Kochanski, & dell'Antonio (1998). This solution required the inclusion of a number of small dark deflecting 'mascons' around each of the lensed images to offset the symmetry of a dominant central potential (see resulting mass distribution in Fig. 2 of Tyson, Kochanski, & dell'Antonio 1998, see also Broadhurst et al. 2000) for which no corresponding cluster members are visible.

A simpler model of this cluster mass-distribution was presented by Broadhurst et al. (2000), by assigning profiles to the brightest cluster members using the form advocated by NFW (Navarro, Frenk & White 1997) in a 16 parameter fit, which reproduced very accurately the 5-image system. This model identified another lensed system comprising two multiple-images, which have been since seen to be of very similar colours and morphology, also in recent deep ACS images. This system is used by Jee et al. (2007) together with the weak-lensing (WL) distortions (Object B1,2 in the notation of Jee et al. 2007) to derive the inner mass distribution based on a non-parametric technique (e.g., Abdelsalam, Saha, & Williams 1998, Diego et al. 2005). Generally, ring-like or monopole degeneracies in such techniques may limit the plausibility of obtaining a reliable solution when only SL data are used to constrain the model (Coe et al. 2008, Liesenborgs et al. 2008a,b). Note that here we found a new counter image of this system on the inner side of the radial critical curve, which was also recently predicted by the model of Liesenborgs et al. (2008b). This is explained in the Results section and is seen Figures 8 and 9.

Strong-lensing modelling methods have improved over the past two decades, in response to computational advances and higher quality data, yet most of these methods still involve many parameters. Most methods can be classified as "parametric" if based on physical parameterisation, and as "non-parametric" if they are "grid-based" (see also §4.4 in Coe et al. 2008, and references therein). Currently, both methods include too many parameters to be well-constrained by the number of initially known multiply-lensed systems. Here we use the deep ACS imaging to identify new multiply-lensed systems, motivated by the successful approach of Broadhurst et al. (2005a) for identifying new multiply-lensed systems with a minimalistic approach to the lens modelling. We present an improved modelling method which involves only 6 free parameters, enabling easier constraint by known systems, since the number of constraints has to be equal or larger to the number of parameters in order to get a reliable fit. Two of these parameters are primarily set to reasonable values and so only 4 of these parameters have to be constrained initially, which sets a very reliable starting-point using the known 5-image system. This we find is sufficient for finding many multiple-images, which are then iteratively incorporated into the model, by using their photo-z estimations to constrain the two initially-set parameters which control the mass profile slope. This will be explained in more detail in §4. Our modelling relies on the reasonable expectation that the mass distribution approximately traces the galaxy distribution and is smoothly varying so we may prefer solutions in which the large scale mass distribution has a minimum of structure. The individual contribution to lensing from the visible galaxies must be included which adds a small well-defined contribution to the overall deflection field. We also compare our resulting mass profile with WL measurements made from deep multi-colour Subaru imaging (Umetsu et al. 2009, in prep) to examine the consistency of the model in the region of overlap.

A major motivation for pursuing accurate lensing-maps is the increased precision of model predictions for cluster-size massive halos in the standard ΛCDM model for the formation (see Umetsu & Broadhurst 2008, e.g., Bullock et al. 2001, Hennawi et al. 2007, Neto et al. 2007, Duffy et al. 2008). Many of the free parameters of this model now rest on a firm empirical foundation with relatively tight constraints on the index and normalisation of the power spectrum of density perturbation and the background cosmological model (see Umetsu & Broadhurst 2008, e.g., Spergel et al. 2003, Tegmark et al. 2004, Spergel et al. 2007).

The standard ΛCDM model is amenable to comparisons with the real Universe via advanced N-body simulations, in particular the recent Millennium simulation (Springel et al. 2005) which simulates a huge volume of $500\text{Mpc}/h$, and has been used to predict the mass function and evolution of nearly 100,000 group and cluster-size CDM halos. Clusters of galaxies and the effects of gravitational potential in them (such as lensing), are good candidates for such comparisons, since there, baryons which are usually omitted from dynamical N-body simulations, are presumed not to have a significant impact on the shape of the cluster gravitational potential (e.g., Blumenthal 1986, Broadhurst & Barkana 2008, Umetsu & Broadhurst 2008). This is because the high temperature of the cluster gas prevents efficient cooling and hence the majority of baryons simply trace the gravitational potential of the dominant dark matter (see also Umetsu & Broadhurst 2008). Massive clusters are of particular interest in the context of this model, because they are predicted to have a distinctively shallow mass profile (or low concentration) described by the form proposed by Navarro, Frenk, & White (1997).

In earlier papers we have explored the combination of weak and strong lensing with new methods designed to achieve the maximum possible lensing precision, combining all lensing information (Broadhurst et al. 2005a,b, Medezinski et al. 2007, Broadhurst et al. 2008, Umetsu & Broadhurst 2008), applied initially to A1689 and then expanding to several other massive well-known clusters with similarly

high quality data. In Broadhurst et al. (2005b) we developed a model-independent method (see also Umetsu & Broadhurst 2008) for reconstructing the cluster mass profile using azimuthally-averaged WL shape distortion and magnification bias measurements, in the wide-field Subaru images. This together with many multiple images identified in deep *Hubble Space Telescope* (HST) Advanced Camera for Surveys (ACS) imaging, defined a detailed lensing-based cluster mass profile, out to the cluster virial radius ($r \sim 2h^{-1}$ Mpc). The combined strong and weak lensing mass profile has been well fitted by an NFW profile (Navarro, Frenk, & White 1997) with high concentration of $c_{\rm vir} \sim 13.7$. This value is significantly larger than theoretically expected ($c_{\rm vir} \simeq 5$) for the standard ΛCDM model (Bullock et al. 2001, Neto et al. 2007, Duffy et al. 2008), even after accounting for expected projection bias (Oguri et al. 2005, Hennawi et al. 2007, Corless, King & Clowe 2008). While this discrepancy is weakened when various inherent modelling and simulation uncertainties are taken into account (Sadeh & Rephaeli 2008), it still raises serious questions regarding the basic assumptions behind the ΛCDM model.

This tendency for higher concentrations than expected by the ΛCDM model, is confirmed also in our recent lensing measurements of four other well-known clusters which all have WL profiles very similar to A1689, and for which the concentrations lie in the range $8 < c_{\rm vir} < 12$ (Broadhurst et al. 2008). In addition, independent information on the internal dynamics of A1689 from over 1000 galaxy spectra (Lemze et al. 2008b) and deep X-ray data (Lemze et al. 2008a) independently support the high concentration claimed for A1689. Other work is also establishing high concentration profiles as this norm for galaxy clusters, which includes other well studied clusters (Gavazzi et al. 2003, Kneib et al. 2003, Oguri et al. 2009), samples of X-ray selected clusters (Duffy et al. 2008), and clusters with large Einstein radii (Broadhurst & Barkana 2008). This is very significant since similarly large Einstein radius (and high concentration-parameter) clusters, would require an earlier formation of the large scale structure than implied by the standard ΛCDM model (Sadeh & Rephaeli 2008).

The paper is organised as follows: In §2 we describe the observations. In §3 we describe the photometry procedure and its processing for obtaining photometric redshifts. In §4 we detail the modelling method and its implementation. We characterize the model, and explain how it was constrained and the verification criteria it obeys. In §5 we report and discuss the results, particularly the newly-discovered multiply lensed systems and the mass distribution. In §6 we summarize and conclude this work.

Throughout this paper, we use the AB magnitude system, and adopt a concordance ΛCDM cosmology with ($\Omega_{\rm m0} = 0.3$, $\Omega_{\Lambda 0} = 0.7$, $h = 0.7$). With these parameters one arcsecond corresponds corresponds to the physical scale of 5.3 kpc/h_{70} for this cluster. The reference centre of our analysis is fixed at the centre of the cD galaxy: RA = 00:26:35.7, Dec = +17:09:43.1 (J2000.0).

2   OBSERVATIONS AND TARGET SELECTION

Observations of this cluster were performed in the framework of the ACS Guaranteed Time Observations (GTO)

which includes deep observations of several massive, intermediate-redshift galaxy clusters. As mentioned in Broadhurst et al. (2005a), some important aims of the GTO program are determination of the mass distribution of clusters for testing the standard cosmological model and to study distant, background lensed galaxies for which some of the very highest redshift galaxies are known because of high magnification by massive clusters (Franx et al. 1997, Frye & Broadhurst 1998, Frye , Broadhurst & Benítez 2002, Kneib et al. 2004, Stark et al. 2007, Bouwens et al. 2008, Bradley et al. 2008, Zheng et al. 2009).

Although the SL by Cl0024+1654 has been analysed before, only two multiple-image systems are currently known in this cluster, including the classic 5-image system (Smail et al. 1996, Colley, Tyson & Turner 1996) and a pair of fainter images identified in WFPC-2 data by the model of Broadhurst et al. (2000). One more multiple system is claimed by Jee et al. (2007), which is discussed later in §5.

The relatively large Einstein radius of this cluster of $\sim 30''$ at a source redshift of $z_s = 1.675$ (corresponding to the 5 image system, Broadhurst et al. 2000) encourages us to search for more such multiple images in our deep GTO imaging. For comparison, in similar quality GTO imaging of A1689, 33 multiply-lensed galaxies were uncovered, forming 106 multiple images for which the Einstein radius is larger, $\sim 45''$ ($z \sim 1.5$). Therefore, taking simply the ratio of the Einstein radius squared, we may expect to detect approximately ~ 13 lensed sources, and where the corresponding number of multiple images depends somewhat on the degree of substructure within the Einstein radius.

Cl0024+1654 was observed in November 2004, with the Wide Field Channel (WFC) of the ACS installed on HST. Integration times of 6435, 5072, 5072, 8971, 10144, and 16328 seconds, were obtained through the F435W, F475W, F555W, F625W, F775W, and F850LP filters, respectively. The NICMOS/NIC3 images of Cl0024+1654 were obtained in 2007 July, with exposures of 9706 seconds in both the F110W and F160W bands. We also used additional archival NICMOS images of this field, taken in 2006 August. The NICMOS images were processed with a custom pipeline (partially based on IRAF scripts) written at the University of California Santa Cruz (NICRED; Magee, Bouwens, & Illingworth, 2007).

3   PHOTOMETRY AND PHOTOMETRIC REDSHIFTS

We obtain $BVg'r'i'z'JH$ photometry from HST ACS and NIC3 (NICMOS C3) images. The ACS images were initially reduced, processed, and analysed by APSIS, the ACS GTO pipeline (Blakeslee et al. 2003). An optimal χ^2 detection image was created as a weighted sum of all filters, each divided by its background RMS. Objects were detected and photometry obtained using SExtractor (Bertin & Arnouts 1996).

SExtractor does well to detect most of our multiple image candidates, but some of the fainter objects elude detection with our choice of parameters. For those objects, we construct apertures "by hand" and use SExSeg (Coe et al. 2006, included in the ColorPro package) to force SExtractor to obtain photometry for those objects.

Other objects are lost in the glare of nearby cluster members. To uncover these objects, we carefully modelled and subtracted the light from most of the cluster galaxies in each of the six filters. First of all, we subtracted the central cD galaxy and its halo from the cluster centre. This was achieved by first masking all the galaxies in the frame, except for the cD galaxy, using SExtractor, and masking manually the small satellite galaxies with an IRAF task built for this purpose, which adopts the shape of the galaxies for the careful masking of their light. Then, we fitted an elliptical model to the cD galaxy with the IRAF tasks ELLIPSE and BMODEL. Afterwards, we subtracted the model from the image and the resultant image was used to estimate and subtract the background and the cD halo with SExtractor. This procedure is iterated until the halo is completely subtracted. Usually, the procedure converges in two iterations (Ascaso et al., in prep.). After that, the surrounding galaxies were fitted into two components by a Sérsic plus exponential profile and therefore their model was again subtracted. The small residua in the final image were also cleaned with SExtractor. This allows us to detect new images (e.g., Figure 9), including faint central demagnified images.

This galaxy-subtraction procedure should improve the photometry (and thus photo-z estimation) for those images close to cluster galaxies. However, the subtraction tends to adversely affect the colours of nearby objects, due to the fact that the best fit model of the cluster galaxies changes its orientation in different bands so it is difficult to model the wings of cluster galaxies in all filters sufficiently well to avoid this.

The ColorPro software is used to ensure robust colours across the ACS and NIC3 images. The NIC3 images are co-registered to the ACS coordinates. Identical photometric apertures are applied to all the aligned images. And corrections are made for broader NIC3 PSF.

Given our $BVg'r'i'z'JH$ photometry, we obtain photometric redshifts using BPZ v1.99.2 (Benítez 2000, Benítez et al. 2004, Coe et al. 2006). The distances to the galaxies are, of course, key ingredients to the lens model. The BPZ analysis also aids us in our multiple image identification, as multiple images should all have the same SEDs (spectral energy distributions).

In Figure 20 we compare the SEDs of the multiple image candidates of each lensed galaxy. We expect good agreement when the images are well isolated, as is the case for images 1.1, 1.3, and 1.4, for example. But some images, such as 1.2 and 1.5, are contaminated by the light from nearby cluster galaxies. We conclude that the photometric redshift estimation for these contaminated galaxies is less reliable, even in the galaxy-subtracted image, as explained above. We can tell which are likely to be contaminated by a visual inspection of the images.

4   STRONG LENSING MODEL

Our aim is to develop a SL modelling method with a minimum of free parameters, so that we have the predictive power to find new multiply-lensed systems. The basic assumption in the construction of the model is that the observed galaxy distribution approximately follows the general DM distribution of the cluster. We assign a fixed power-law profile to cluster member galaxies, of slope q, and scaled linearly in amplitude by the observed brightness. The power law index q is a free parameter of the model. Adding all these profiles together results in a fairly smooth overall mass distribution with local maxima corresponding to each member galaxy. This approach is similar to that of Broadhurst et al. (2005a), which was successfully used to identify over 30 sets of multiple images in similarly deep ACS/GTO imaging of A1689, and also for the more distant cluster SDSS1004+4112 which was discovered to have 4 bright lensed QSO images (Oguri et al. 2004, Inada et al. 2005) and for which 3 sets of new multiply lensed galaxies were identified in deep ACS images (Sharon et al. 2005).

We expect that the DM distribution is smoother than this co-added galaxy distribution and with a much higher overall mass scaling. To represent the DM distribution we interpolate over the above sum of galaxy masses with a low order cubic-spline interpolation and calculate the corresponding deflection field, where the polynomial order of this function is denoted as S, or the *smoothing degree*, which is a free parameter of the model. The scaling of this smooth DM component relative to the total galaxy mass is denoted by K_{gal}, which is another free parameter of the model.

Though the best fitting solutions require a relatively small galaxy contribution compared to the smooth component, the galaxy contribution is, however, not negligible in the sense that lensed images lying near cluster members are locally deflected significantly by them, and hence these must be included in order to correctly identify multiply-lensed images. We denote an additional free parameter of the model as K_q, which as seen in eqs. 1 and 2, is proportional to the lensing distance ratio d_{ls}/d_s, and contains the other constants seen there.

We do not expect the galaxies and DM to trace each other in detail and some flexibility should be allowed. Therefore we simply Taylor expand to first order the potential of the DM distribution, which adds two more free parameters: the shear amplitude, γ, and its position angle ϕ, which together equivalently describe the overall matter ellipticity.

We find that these 6 parameters are sufficient for identifying new multiple images and for defining well the mass profile of the cluster as we show in detail below. This is preferable to the common approach of subjectively defining sub-clusters as separate elliptical masses, with the many attendant extra parameters this entails.

In the process of identifying new images it is important to make use of all the pixel information, and so we delens each set of pixels belonging to an image in each passband back to the source plane to act as the source for generating counter images. These relensed images then reflect the internal colour and morphological structure of the observed lensed candidate galaxy, which is very helpful in uniquely identifying new images. We generate a family of relensed images to cover a range of plausible lensing distances as any image must lie somewhere along a locus defined this way. We now detail the modelling procedure.

4.1   Initial Mass Distribution

A catalogue of the cluster galaxies was created by colour-colour diagrams. The ~ 300 brightest cluster galaxies (within the ACS frame) were chosen in order to construct

the mass distribution. The list includes the centre pixel coordinates of each galaxy and its flux. By assuming a certain M/L ratio, or that the flux is proportional to the mass, the deflection field contributed by each object can now be calculated by assigning a galaxy surface-density profile for each galaxy, $\Sigma(r) = Kr^{-q}$, which is integrated to give the interior mass, $M(< \theta) = \frac{2\pi K}{2-q}(d_l\theta)^{2-q}$. This results in a deflection angle of (due to a single galaxy):

$$\alpha(\theta) = \frac{4GM(< \theta)}{c^2\theta}\frac{d_{ls}}{d_s d_l}. \tag{1}$$

Since $M(< \theta) \propto \theta^{2-q}$, and since we assume a certain M/L relation according to which the flux, F, is proportional to the mass, we can reduce the latter formula to get:

$$\alpha(\theta) = K_q F\theta^{1-q}, \tag{2}$$

where K_q is a new defined constant which contains all previous constants and the proportion relations, and it is dependent also upon the power-law index, q.

The deflection angle in a certain point $\vec{\theta}$ due to lumpy galaxy components is simply a linear sum of each galaxy contribution, summed over all i galaxies:

$$\vec{\alpha}_{gal}(\vec{\theta}) = K_q \sum_i F_i\, |\vec{\theta} - \vec{\theta}_i|^{1-q}\, \frac{\vec{\theta} - \vec{\theta}_i}{|\vec{\theta} - \vec{\theta}_i|}. \tag{3}$$

A discretised version of equation (3) over a two dimensional square grid $\vec{\theta}_m$ of $N \times N$ pixels is given by:

$$\alpha_{gal,x}(\vec{\theta}_m) = K_q \sum_i F_i\, \left[(\Delta x_{mi})^2 + (\Delta y_{mi})^2\right]^{-q/2} \Delta x_{mi}, \tag{4}$$

$$\alpha_{gal,y}(\vec{\theta}_m) = K_q \sum_i F_i\, \left[(\Delta x_{mi})^2 + (\Delta y_{mi})^2\right]^{-q/2} \Delta y_{mi}, \tag{5}$$

where $(\Delta x_{mi}, \Delta y_{mi})$ is the displacement vector $\vec{\theta}_m - \vec{\theta}_i$ of the mth pixel point, with respect to the ith galaxy position $\vec{\theta}_i$.

From this a deflection field for the galaxy contribution is easily calculated analytically as above, and the mass distribution is now rapidly calculated locally from the divergence of the deflection field, i.e., the 2D equivalent of Poisson's equation.

4.2   The Dark Matter Distribution

The mass contribution of galaxies, described above, is anticipated to comprise only a small fraction of the total mass of the cluster, which is expected to be dominated by a smooth distribution of DM. We now simply assume that the galaxies approximately trace the dark matter. This assumption was found to work well in earlier work on this cluster and on A1689 (Broadhurst et al. 2000, Broadhurst et al. 2005a) where an unprecedented number of multiple-images were found (Broadhurst et al. 2000, Broadhurst et al. 2005a). Since the DM is of course expected to be smoother than the distribution of galaxies, we smooth the initial guess of the DM distribution obtained above, choosing for convenience a low-order cubic spline interpolation.

The smoothing degree (the polynomial degree, S) is also a free parameter of the model. The deflection field of the DM is then (where each pixel is a δ-function mass distribution):

$$\alpha_{DM,x}(\vec{\theta}_m) = K_q \sum_i P_i\, \left[(\Delta x_{mi})^2 + (\Delta y_{mi})^2\right]^{-1} \Delta x_{mi}, \tag{6}$$

$$\alpha_{DM,y}(\vec{\theta}_m) = K_q \sum_i P_i\, \left[(\Delta x_{mi})^2 + (\Delta y_{mi})^2\right]^{-1} \Delta y_{mi}, \tag{7}$$

where P_i represents the mass value in the ith pixel. Thus we obtain now the deflection field due to the DM, hereafter $\vec{\alpha}_{DM}(\vec{\theta})$, or the *smooth component*.

4.3   The Initial Deflection Field

After obtaining the two components of the deflection field, we now simply add them together to get a total deflection field as follows:

$$\vec{\alpha}_T(\vec{\theta}) = K_{gal}\vec{\alpha}_{gal}(\vec{\theta}) + (1 - K_{gal})\vec{\alpha}_{DM}(\vec{\theta}), \tag{8}$$

where K_{gal} is the relative contribution of the galaxy component to the deflection field.

4.4   External Shear

Since the assumption that the DM follows the galaxies light or mass is not expected to be rigorous in detail, allowance should be made for the unknown DM distribution to differ somewhat from the light, particularly on large scales where the influence of mass outside the central region may be important through tidal interaction. Various ways have been used before, among them matching a high-order polynomial which would fine-tune the DM distribution (e.g., Broadhurst et al. 2000, 2005a). However, we find that adding an external shear, or equivalently a large scale ellipticity (e.g., Kovenr 1987a,b, Keeton, Kochanek, & Seljak, 1997, and references therein) provides considerable flexibility and adds only two additional free parameters, if we only Taylor expand the potential to first-order. Note that this is also "safer" than other methods since it relies on physical considerations alone. Thus, the total deflection field is now given by:

$$\vec{\alpha}_T(\vec{\theta}) = K_{gal}\vec{\alpha}_{gal}(\vec{\theta}) + (1 - K_{gal})\vec{\alpha}_{DM}(\vec{\theta}) + \vec{\alpha}_{ex}(\vec{\theta}), \tag{9}$$

where the deflection field at position $\vec{\theta}_m$ due to the external shear, $\vec{\alpha}_{ex}(\vec{\theta}_m) = (\alpha_{ex,x}, \alpha_{ex,y})$, is given by (see also Kovenr 1987a,b, Keeton, Kochanek, & Seljak, 1997, and references therein):

$$\alpha_{ex,x}(\vec{\theta}_m) = |\gamma| \cos(2\phi_\gamma)\Delta x_m + |\gamma| \sin(2\phi_\gamma)\Delta y_m, \tag{10}$$

$$\alpha_{ex,y}(\vec{\theta}_m) = |\gamma| \sin(2\phi_\gamma)\Delta x_m - |\gamma| \cos(2\phi_\gamma)\Delta y_m, \tag{11}$$

where $(\Delta x_m, \Delta y_m)$ is the displacement vector of the position $\vec{\theta}_m$ with respect to a fiducial reference position, which we take as the lower-left pixel position $(1, 1)$, and ϕ_γ is the position angle of the spin-2 external gravitational shear measured anti-clockwise from the x-axis.

4.5   The Magnification and Critical Curves

The magnification can be calculated simply from the gradients of the above deflection field. The magnification at a given position (see Narayan, & Bartelmann 1996, Broadhurst et al. 2005a, and references therein), $\mu(\vec{\theta})$, is given by the Jacobian of the lens mapping and can be expressed by the derivatives of the deflection field:

$$\mu(\vec{\theta})^{-1} = 1 - \vec{\nabla} \cdot \vec{\alpha} + \alpha_{x,x}\alpha_{y,y} - \alpha_{x,y}\alpha_{y,x}, \qquad (12)$$

where $\vec{\alpha}(\vec{\theta})$ and its derivatives refer to the total deflection field (now containing also the external shears), $\vec{\alpha}_T(\vec{\theta})$, and its derivatives, respectively. It should be noted that $\alpha_{x,y} = \alpha_{y,x}$ because the deflection field is curl free. After constraining the model parameters, we calculate the magnification field using the above equation, which depends on the source distance, via the lensing distance ratio, d_{ls}/d_s. The relative magnifications are used later as a consistency check of our modelling, by comparison with the independent relative flux information for the multiply-lensed images.

4.6 Iteration process

We have found that the search for an adequate SL model can be divided conveniently into two stages of iteration. The first stage (hereafter the *internal iteration*), is to constrain the parameters - K_q, K_{gal}, γ, and ϕ_γ. The slope determining parameters, q and S, are first held fixed at reasonable values, since these parameters are not strongly constrainable at this point, until we have identified new lensed systems and incorporated their photo-z measurements to break the mass-sheet degeneracy and thereby obtain a useful measure of the gradient of the mass profile. We start by minimising as above from de-lensing only the 5-image system, fully constraining these 4 internal parameters. For this internal iteration, we find a source plane iteration is sufficient to begin our search for new multiply-lensed systems. This minimisation is efficient and allows us to search exhaustively in an interactive way for new multiply-lensed systems, using each pixel information as described above. The properties of the new multiply-lensed systems, including photo-z estimations, are outlined in the Results section and listed in Table 1.

Having obtained new multiple images this way we have discovered that we can make use of their photo-z information to meaningfully constrain the slope of the mass profile. We generate a grid of values covering a wide range of q and S. We now obtain the best fit by minimising the model solution per each predetermined combination of these parameters, incorporating the photo-z estimations of these new systems. This we name the *outer iteration*. We maintain the minimisation in the image-plane in order to avoid the inherent bias towards shallower mass profiles when relying on source-plane minimisations. We also check that all the observed images are reproduced in this process and also examine for consistency the relative image brightness compared with the model-predicted relative magnifications. In Figures 1 to 4 we show the effects of different q and S values on the resulting mass profile and the magnification profile.

By using the following lens equation (eq. 13) one can lens images back onto the source plane, and re-lens the source into the lens plane:

$$\vec{\theta} = \vec{\beta} + K_q\vec{\alpha}_T(\vec{\theta}), \qquad (13)$$

where K_q is now scaled so it corresponds to the observed locations of the images of each system.

4.6.1 The Image Plane RMS

We relens the images of likely lensed galaxies in our search for counter images, using all the pixel information as de-scribed in the beginning of §4. We measure the RMS of the reproduced images with respect to their observed locations to measure the fit:

$$RMS_{images}^2 = \sum_i (x_i' - x_i)^2 + (y_i' - y_i)^2 \ / \ N_{images}, \qquad (14)$$

where x_i' and y_i' are the locations given by the model, and x_i and y_i are the real images location, and the sum is over all N_{images} images. Each system was minimised to its best reproduction.

The effect of different q and S on the image reproduction can be generally described as follows: for a fixed smoothing degree S, a shallow galaxy mass profile (lower q) generates too shallow a cluster mass profile, resulting in a higher magnification that generally predicts extra unobserved images (see Figures 1 to 4). On the other hand, too high a value of q steepens the cluster mass profile, resulting in a lower magnification and generally does not reproduce all the observed images. For a fixed q, too low a smoothing degree S produces slightly too shallow a mass profile (meaning slightly higher magnification), but more significantly the matter distribution is then not detailed enough in its internal structure and therefore generally underpredicts the number of observed images, or generates images with incorrect orientation or twisted internal shape. A too high smoothing degree S produces a slightly too steep a mass profile and too detailed a mass distribution, resulting in extra or missing images, or images with twisted shapes.

4.6.2 The Comparison to photo-z's

We examine the growth of the model scaling factor K_q versus the expected growth of d_{ls}/d_s with source redshift, based on the standard cosmological relation. The difference between the predicted and measured redshifts is then characterised by:

$$RMS_z^2 = \sum_i (z_i^{model} - z_i^{photo})^2 \ / \ N_{systems} \qquad (15)$$

where the sum is over the number of systems used here, $N_{systems}$. However, since the model-predicted redshifts are manifested in the scaling factor K_q, this formula can be expressed in terms of this factor:

$$RMS_{K_q}^2 = \sum_i (K_{q,i}^{model} - K_{q,i}^{photo})^2 \ / \ N_{systems}. \qquad (16)$$

The effect of varying the profile with q and S, on the photo-z predictions can be generally described as follows: for a fixed smoothing degree S, a too shallow galaxy mass profile (lower q) results in a shallower mass profile (see Figure 1) which "compresses" the range of photo-z compared to the cosmological relation, so that we underestimate the redshift of systems which exceed the reference z=1.675, for which $K_q > 1$, and overestimate the redshift of systems which lie below z=1.675, for which $K_q < 1$. On the other hand, choosing too high a value of q corresponding to too steep a profile has the opposite effect of "expanding" the range of predicted photo-z's compared with the cosmological expectation. Note that the exact choice of cosmology is not at all important, all the predicted curves look alike, as unfortunately the variation of the lensing distance ratio, d_{ls}/d_s, is relatively insensitive to cosmology as shown in Figure 27.

4.6.3 The Comparison of Relative Magnifications

The relative magnification of different images of a system also provides a consistency check for the model. Since gravitational lensing preserves surface brightness, both the total flux from each image and the area of each image of a source are proportional to the magnification at the image position. Therefore the ratio between the fluxes (or the areas) of two images of a source should be the same as the model magnification values at the image positions, and this can be used to check the model.

In order to quantify the discrepancy of the relative magnification we use the following procedure: we denote F_1 and F_2, as the measured fluxes of two images of the same system, and m_1 and m_2 as the magnification values at these image positions. By definition, $F_1 = F \cdot m_1$ and $F_2 = F \cdot m_2$, where F is the same original flux and it is therefore identical for both images of the same system. The model-predicted magnitude difference of these images ($\Delta mag = mag1 - mag2$) is therefore given by:

$$\Delta mag = -2.5(logm_1 - logm_2). \tag{17}$$

We use the latter equation to calculate the RMS of the relative magnification, by comparing the measured magnitude difference to the latter model-predicted value. This is obtained by:

$$RMS^2_{mag} = \sum_i (\Delta mag^{meas.} - \Delta mag^{model})^2 \ / \ N_{images}, \tag{18}$$

where the sum is over all images, and each magnitude difference is calculated with respect to the first image of the corresponding system of the image.

As can be seen from Figures 1 to 4, the magnification is very sensitive to the mass profile: relatively small changes in the mass steepness will result in much higher changes in the magnification (and relative magnifications). A higher q and S form a steeper profile for which both the magnification and the relative magnifications are higher, and vice versa. Due to the entanglement to the photo-z comparison criterion, the relative magnifications are used only as a consistency check of our best model (see next subsection).

4.7 Constraining the Mass Profile

We stressed in the preceding sections that only broad constraints on the gradient of the mass profile are feasible using just the locations of the multiply-lensed images alone, and that a tighter constraint on the slope-determining parameters q and S comes from incorporating the cosmological redshift-distance relation. This is done by applying the lensing distances of each system based on the measured photo-z's.

We now wish to select the solutions for which the d_{ls}/d_s model-estimates lie closest to the expected cosmological relation (see also §4.6.2). This will then allow us to define better the gradient of the mass profile, as previously mentioned. In so doing we concentrate in particular on the $z \simeq 4$ system (system number 8), which is our most distant multiple-image system and for which the photometric redshift estimation is unambiguous and relatively accurate due to the marked break in the SED (Figure 20), corresponding to the Lyman limit and intervening Lyman forest absorption.
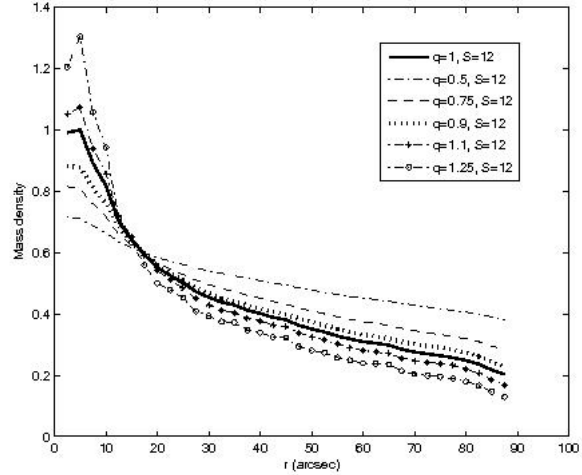
Figure 1. Comparison of different mass density profiles as a function of q, where the peak mass densities are normalised to the case $q = 1$. The centre is slightly shifted to better see the limit each profile peaks to.
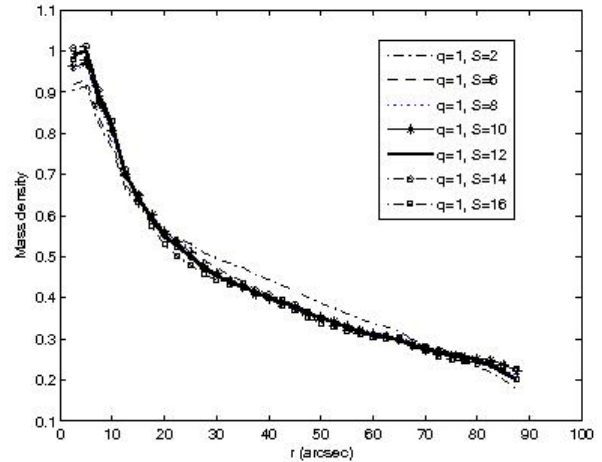

Figure 2. Comparison of different mass density profiles as a function of S for fixed q. The mass density is normalised as before. The centre is slightly shifted to better see the limit each profile peaks to.

Finding the best fitting combinations of q and S is straightforward since too shallow a slope leads to an underestimate of the redshift of the $z \simeq 4$ system, and too steep a slope overestimates it (as detailed in §4.6.2). This is because, as can be seen in Figures 1 and 2, a higher q, and to a lesser extent a higher S, would result in a steeper overall mass profile, and vice versa. The best fitting solution lies near $q=1.3$, $S=10$, with some degeneracy between q and S, which is not that physically important as the parameters
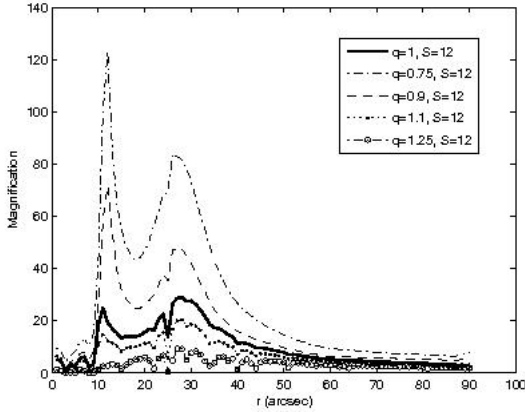
Figure 3. Comparison of different magnification profiles, as a function of q, for fixed S. Notice the radial and tangential critical radii which are distinctive for low q models.
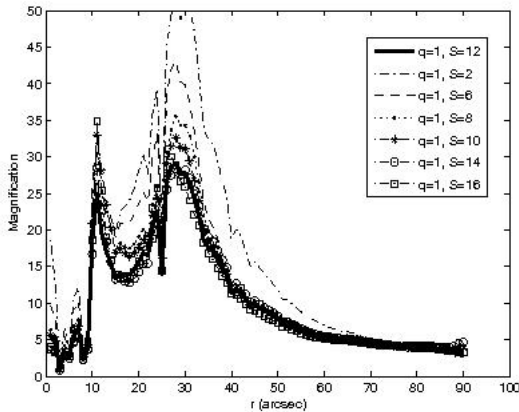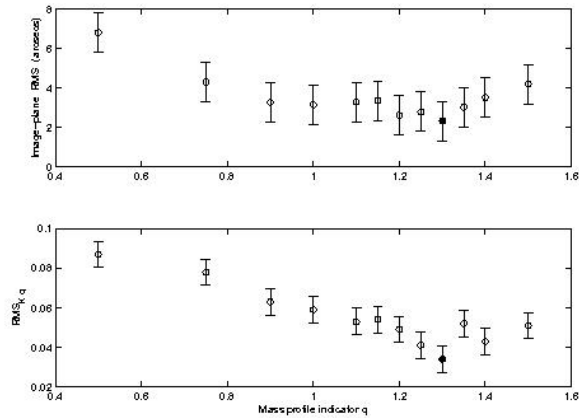

Figure 5. Top: typical image-plane RMS as a function of q. Bottom: typical RMS_{K_q} as a function of q. A minimum is seen around a value of $q \simeq 1.3$ in both cases, but it is clear that the minimum is better defined by the use of photometric redshifts, in terms of RMS_{K_q}.

obtain a similar best-fitting value of q, the minimum is not as clear.

In Table 1 we also include the relative magnifications comparison of the best model as a consistency check. Here we also see good consistency with the best fitting model ($RMS_{mag} \sim 0.5\ mag$), with the data lying very closely along the equality slope (Figure 28), with the scatter increasing symmetrically with increasing magnitude. The most discrepant point (lower right) is one of the images of system 7 for which the photometry is difficult due to its anomalously low surface brightness and for which the predicted redshift, given the cosmological relation, is not matched by our photo-z estimated redshift.

We now show in the next section a comparison between the predicted images and their model-generated images (for the best-fitting model), in order to demonstrate the plausibility of our solution both in terms of the appearances of the images and their photometric redshifts.

Figure 4. Comparison of different magnification profiles, as a function of S, for fixed q.

combine so that any solution near this position generates a very similar mass profile (see Figure 6).

We then examine how well the cosmological relation is reproduced accounting also for the other systems with reliable photo-z measurements (9 in total), as shown in Figure 5 (bottom). Note that the best fitting model as obtained from system 8 above is also in best agreement with the redshift estimates of all the 9 systems together. Clearly the redshift estimates for these systems verify very well that the predicted deflection (K_q) of the best fitting model at the estimated redshifts of each of these 9 systems lies precisely along the expected cosmological relation, as seen in Figure 27, with a mean deviation of only $RMS_{K_q} \sim 0.03$ for the best model, considerably strengthening the plausibility of our approach to modelling in general. Note that if we rely only on the image locations, Figure 5 (top), although we

5   RESULTS AND DISCUSSION

In this section we present the new multiple-image systems found by the model, the derived mass distribution and profile, and the resulting magnification. We also make consistency checks of our model using independent information including photometric redshifts, relative fluxes, WL data, and a comparison to an NFW profile.

5.1   Multiply-Lensed Systems and Candidates

Here we discuss the various multiply-lensed systems. Each system identified with the help of the model is presented and accompanied by modelled images of the same system. Each image is relensed using all the pixel information contained in one of the counter images, so that each modelled
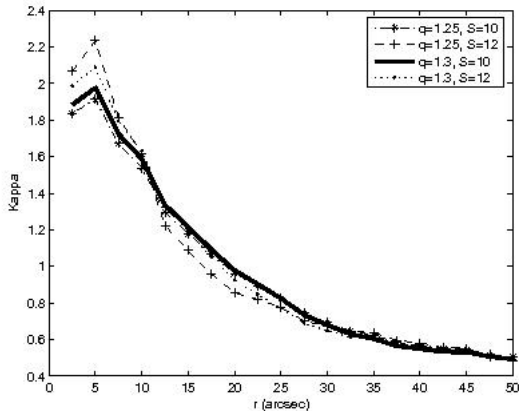
Figure 6. Mass profiles of the best-fitting model (solid curve). The dashed curves indicate the profiles of three other solutions which differ by $\sim 1\,\sigma$ from the best solution, in terms of both slope controlling parameters q and S. The y-axis is the lens convergence, κ (which is proportional to the mass density), where for a source of $z = 1.675$ behind this cluster $\Sigma_{crit} = 0.47\ g/cm^2$. The x-axis is the radius from the cD galaxy in arcseconds, where each arcsecond equals 5.3 kpc/h_{70}.

Figure 7. System number 1: Five images of the well known "Theta"-arc are displayed in the top row (1.1 to 1.5), including the central radial arc, 1.2, with the best-fitting model reproduction shown below. All model images are based on our delensing-relensing technique, allowing for the most detailed comparison possible given the resolution of the data. The reproduction of images 1.3 and 1.5 is somewhat complicated by the presence of nearby cluster member galaxies, whose mass profiles will be interesting to explore further. The photometrically determined redshift probability distribution based on our optical-IR measured photometry is shown below. Note that images 1.2 and 1.4 are significantly affected by nearby light from cluster member galaxies (see Figure 20), badly affecting their photometric redshift estimation, whereas image 1.1, 1.3 and 1.5 predict a photometric redshift of, $z = 1.45 \pm 0.25$, (Table 1) in agreement with the measured redshift of $z = 1.675$ (Broadhurst et al. 2000).

image is the relensed counter-image of another image of the same system. This detailed modelling of the images is shown together with the photometric redshift probability function of each image, so that the precision and uniqueness of the photometric redshift can be assessed.

All systems are summarised in Table 1, and are marked on a colour image along with the critical curves (see Figure 21). The model reproduces quite accurately nearly all lensed galaxy images, with respect to their locations ($RMS \sim 2.5''$) and redshift ($RMS_{K_q} \sim 0.03$), as well as their shape and relative magnification ($RMS_{mag} \sim 0.5\ mag$). In the few cases where there is ambiguity in one or more of the counter images we present the alternative possibility together with the favoured identification. It should be noted however that this degeneracy does not alter the mass distribution as these alternative counter images lie very close to each other.

*System*1: This is the historically well-known system, consisting of five images, first noted by Koo (1988). Three of these images were resolved into a close triplet of arcs (Kassiola, Kovner, & Blandford, 1992; images 1.3, 1.4, and 1.5 in Figure 7 here), where the two additional images (1.1 and 1.2) were later also classified as members of this system (e.g., Smail et al. 1996, Colley, Tyson & Turner 1996). This system is the only multiply-lensed system in this cluster which has a spectroscopic redshift ($z = 1.675$, Broadhurst et al. 2000). We therefore use this system for the internal minimisation of the model, which sets the scaling factor K_q to 1 for this system. In Figure 7 we show the five images of this system in the ACS colour image, their reproduction by the model, and the photo-z distribution of each image. The images are accurately reproduced by the best fitting model (Figure 7). Note that next to image 1.4 two small spots are reproduced but if they are realistic and not a lensing noise effect, they are hidden behind the bright galaxies seen in
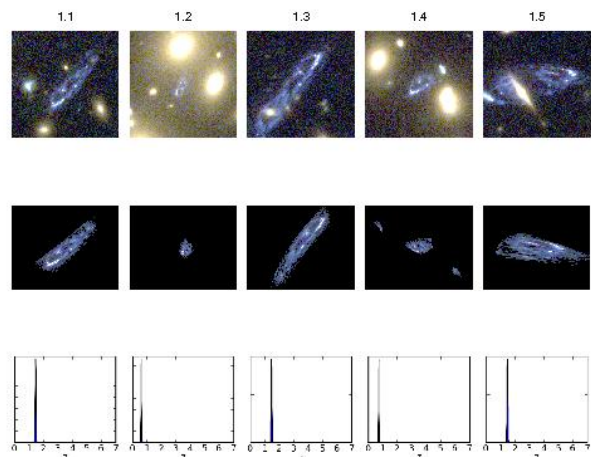
the same figure. The photo-z's of the bright images (1.1, 1.3 and 1.5) agree well with each other ($z \simeq 1.45 \pm 0.25$, see Table 1), and with the spectroscopic redshift ($z = 1.675$). The two fainter images (1.2 and 1.4), both lie next to bright cluster galaxies, influencing their photometry and therefore their photo-z is unreliable (Table 1).

*System*2: We identify three images for this system (Figure 8), two of which were first proposed by Broadhurst et al. (2000) based on shallow WFPC-2 images. These images were later observed to have very similar internal colours and structure in deep ACS images and were used by Jee et al. (2007). Our model confirms these images to be members of the same system and predicts a third radial image, 2.3, lying just inside the radial critical curve, revealed for the first time in a galaxy-subtracted image made by us (Figure 9). This additional radial image was predicted also in recent work by Liesenborgs et al. 2008b. The SEDs of images 2.1 and 2.2 are very similar (Figure 20). Images 2.2 and 2.3 are radially directed, and have opposite parity, indicating that they lie on opposite sides of the radial critical curve in agreement with our model prediction. Our best fitting model predicts a redshift of $z = 1.22 \pm 0.1$ for this system in good agree-
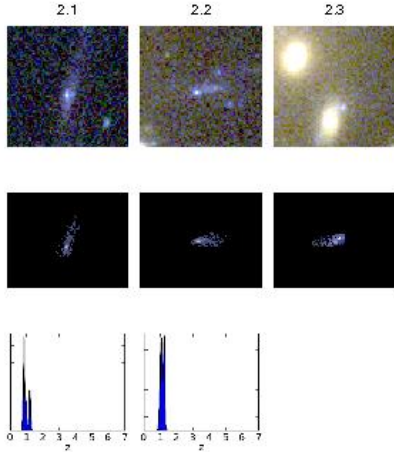
Figure 8. System number 2: The three images of this system are shown in the top row, where below them we add the model-reproduced images. The third row is the photo-z distributions of the images which agree with our $z \sim 1.2$ prediction. Note that image 2.3 lacks photometric redshift as it is hidden in a bright cluster galaxy. Images 2.1 and 2.2 were first identified as a multiply-lensed system by Broadhurst et al. (2000), where image 2.3 was predicted recently by Liesenborgs et al. (2008b), and was found here (see also Figure 9). Note that images 2.2 and 2.3 lie on two sides of the radial critical curve and show opposite parity.

ment with the estimated value of $z = 1.24$ by our photo-z analysis, combining the estimates of images 2.1. and 2.2.

*System*3: This system comprises four blue images with a similar lumpy internal substructure. The predicted redshift from our lensing model is $2.55^{+0.45}_{-0.20}$ where photo-z's of these images range from $z = 2.48$ to $z = 2.76$ (Table 1), in good agreement with the model. One image (3.1 in Figure 10) appears in the south-eastern side of the cluster, opposite to the three other images on the north-western side. These images have very similar SEDs as can be seen in Figure 20. It should be noted that images 3.1 and 3.4 are close to images 5.2 and 5.1, respectively, and show similar colours (to the eye). This might imply a certain degeneracy between these systems. However, an inspection of these systems SEDs (Figure 20) and photo-z distribution, supports the model-prediction that these systems are multiply-lensed in the form presented here. In addition, the system 5 SEDs were compared to the mean system 3 SED. The former are steeper and, based solely on the photometric uncertainties, disagree with the latter with $\chi^2 = 3.4, 3.6$ ($\sim 93\%$ confidence). Contamination from nearby neighbors may also contribute to SED disagreement in general, though these galaxy images appear fairly well isolated.

*System*4: Images 4.1 and 4.2 are very close to each other and relatively close to the cluster centre, and lie on the opposite sides of the radial critical curve next to cluster galaxies, and therefore are highly magnified. The third image, 4.3, is on the other side of the cluster, and it is less magnified, as can be seen in Figure 11. The internal structure is very well reproduced by our model, in particular the location of the
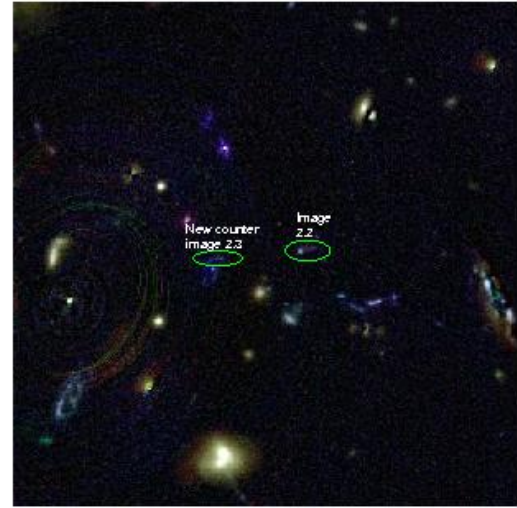

Figure 9. Newly-revealed radial image of system number 2, along with its counter radial-image. The cluster galaxies were subtracted from the image, revealing image 2.3.
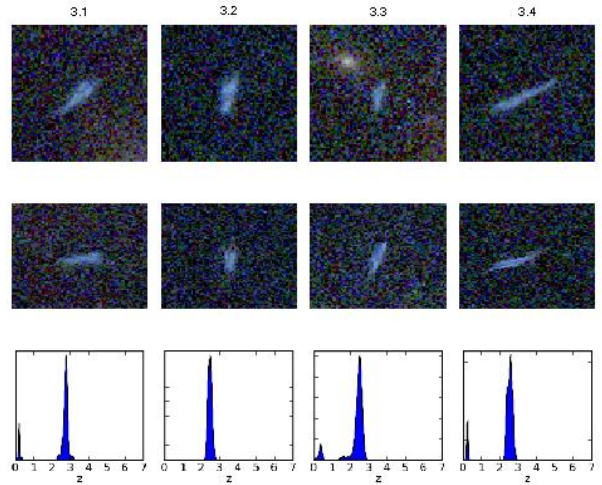

Figure 10. System number 3: The four images of this system are shown in the top row, where below them we add the model-reproduced images on similar artificial background. The third row is the photo-z distributions of the images which agree with our $z \sim 2.6$ prediction.

white knot relative to the diffuse blue emission. The lensing model predicts a redshift of 1.96 ± 0.2, similar to the photo-z estimate of $z \sim 2.2$. Note that for image 4.1 there is no IR data since it lies outside the region covered by NIC3. The SEDs of images 4.1, 4.2, and 4.3 (Figure 20) have a similar
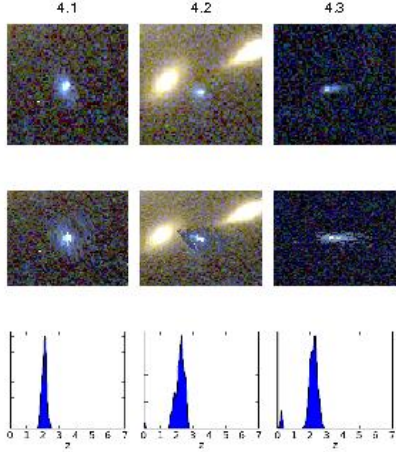
Figure 11. System number 4: The three images of this system are shown in the top row, where below them we add the model-reproduced images. The third row is the photo-z distributions of the images which agree with our $z \sim 2$ prediction. Images 4.1 and 4.2 lie on the two sides of the radial critical curve, and are locally lensed by cluster members which further magnify them.

Figure 12. System number 5: The two images of this system are shown in the top row, where below them we add the model-reproduced images on similar artificial background. The third row is the photo-z distributions of the images which agree with our $z \sim 2$ prediction.

shape in the optical, but image 4.2 is slightly brighter in the red, due to contamination by nearby cluster members.

System 5: Two blue images, seen in two different sides of the cluster. Both images have similar structure as can be seen in Figure 12, and the model-predicted counter images generated by relensing each of these images for comparison with the other, look very much like the observed images. Also, both images have similar SEDs (Figure 20). Image 5.1 lies right on the boundary of the IR coverage and so we restrict the photo-z estimate only to the optical data in both cases. This produces a photo-z of $z = 2.02$ for both images, which accurately fits the lensing model which predicts $z = 2.02^{+0.10}_{-0.10}$. Note that this redshift agrees also with the IR-included photo-z as it is bimodal (see Figure 12).

System 6: Image 6.1 is a radial arc next to a bright central cluster member, whereas its companion is revealed on the other side of the cluster. Due to the proximity to the cluster member, the SED of image 6.1 is badly affected. The photo-z distribution of image 6.2 is bimodal, with the higher redshift peak at $z \simeq 2$ in agreement with our lensing model which predicts $z = 1.93^{+0.15}_{-0.12}$ for this system, whereas the lower redshift photo-z peak at $z = 0.46$ is too low to produce a counter image and therefore excluded. Note that in Jee et al. (2007), the radial arc (image 6.1 in Figure 13) was proposed to match with a counter image on the same side of the lens as image 6.1, which is physically impossible in the context of our model. It should also be noted that there are two similar looking arcs seen in the vicinity of image 6.2, yet these are excluded via SEDs and photo-z comparison.

System 7: Two large, low-surface-brightness and slightly reddish images, lying on opposite sides of the cluster. Though somewhat too faint to be easily noticed in Figure 14, a close inspection by eye in a high resolution colour image shows the colour and shape resemblance. The lensing model
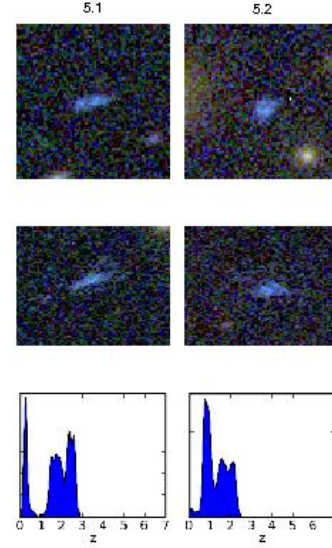
reproduced the locations and shape of these images well, at a best fitting redshift of $z = 2.15^{+0.28}_{-0.26}$. However, the photometric redshift is not in close agreement with this prediction low, $z \sim 1$, see Table 1. The SEDs of these images are relatively similar but with relatively large photometric errors (due to the images being faint). We do not trust the photo-z prediction in that case and conclude that it is plausible that the rather red SED of this system may be significantly affected by extinction, and that for such objects we lack suitable templates for a reliable photo-z determination.

System 8: Two green images, the first (8.1) is a tangential arc ~ 50" from the cluster centre. The second (8.2) falls on the other side of the cluster, closer to the centre. Photometric redshifts predict $z = 4.09$ and $z = 4.16$ for these images respectively, in agreement with our lensing model which predicts a similar redshift of $z = 4.03 \pm 0.5$. Also, the SEDs of these images look very similar (Figure 20) with the characteristic break expected of a distant drop-out galaxy. Note that one image (8.1) lacks NIC3 coverage.

System 9: Images 9.1 and 9.2 (Figure 16) are probably two different images, straddling the radial critical curve. Their counter image (9.3) is a small bright spot, which has a similar SED (Figure 20). This configuration is given for a source redshift of $z \sim 2$, according to the lensing model. Note that this does not agree with the photo-z estimation for images 9.1 and 9.2 ($z \sim 3.4$), which is significantly affected by the nearby bright cluster member. The photo-z distribution of image 9.3 is bimodal, with the higher redshift option lying in the range $z \sim 2 - 3.5$, in agreement with our lensing model. Note that in the vicinity of image 9.3 there is another small arc with a bright spot (RA=00:26:37.85,
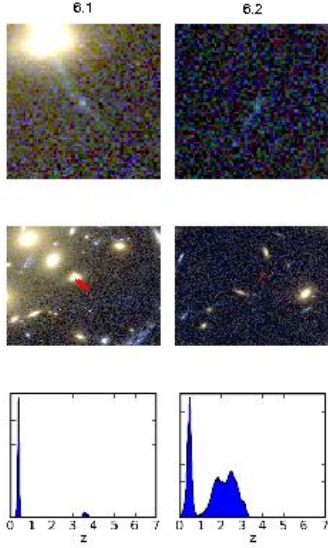
Figure 13. System number 6: The two images of this system are shown in the top row, where below them we add the model-reproduced images. The third row is the photo-z distributions of the images. Note that due to the vicinity of image 6.1 to a bright cluster galaxy, its photo-z estimate is unreliable. The photo-z distribution of image 6.2 agrees with our model estimate of $z \sim 1.9$. Also, due to the vicinity of image 6.1 to a cluster member, the colour delensing-relensing is seriously contaminated. We therefore lens each image of this system to reproduce its counter image, painted in red to emphasise the accuracy of the model with respect to images location. This is seen in the second row, where we also zoom out in order to better show the relative location of the reproduced images in the cluster.
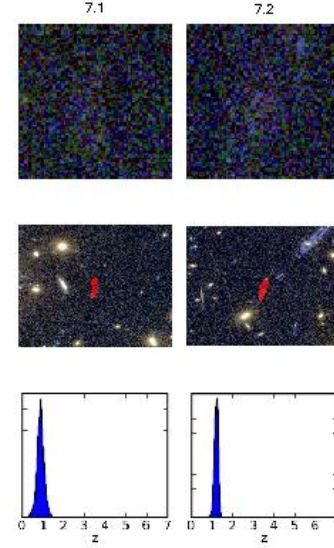

Figure 14. System number 7: The two images of this system are shown in the top row, where below them we add the model-reproduced images. The third row is the photo-z distributions of the images. Note that due to the low surface brightness of these images, their photo-z estimate is unreliable. Our model reproduces these images with a source redshift of $z \sim 2.2$. Being too faint to notice here, we lens each image of this system to reproduce its counter image, painted in red to emphasise the accuracy of the model with respect to images location and general shape. This is seen in the second row, where we also zoom out in order to better show the relative location of the reproduced images in the cluster.

DEC=+17:09:58.54), which has similar SED and might be another option, though it is less supported by our model.

*System*10: Images 10.1 and 10.2 (Figure 17) are two purple-like radial arcs in the cluster centre, probably counter images of one another, lying across the radial critical curve. A third counter image, 10.3, is found on the other side of the cluster. The SEDs and photo-z estimation of images 10.1 and 10.2 are affected by the halo of bright cluster members. The photo-z of image 10.3 is $0.85^{+0.31}_{-0.26}$, in good agreement with our lensing model prediction of $z = 0.96^{+0.23}_{-0.20}$.

*System*11: This system imitates the location of the main 5-image system, with a slightly larger radius (and therefore redshift) comprising four blue images with internal bright spots, next to images 1.1, 1.3, 1.4 and 1.5, respectively, and well reproduced by our model. A very small image is predicted in the cluster centre near 1.2, but was not found, probably due to the bright member light and uncertain subtraction at the predicted location. All images show very similar SEDs. The model predicts a redshift of z=2.50 ± 0.5 for this system, where photo-z analysis shows an agreeing redshift of $z \sim 2.8$.

To summarize, all the multiply-lensed are well reproduced by the model, with respect to their location, shape and photo-z. Note that the various images within each

system have similar SEDs, where not strongly affected by galaxy light. All images are summarised in Table 1.

5.2 Magnification Map and Critical Curves

The magnification value at each point determines how magnified a lensed image would be were it to appear at that point. We compare the relative magnitudes of various images of the same system to the same relative-magnification predicted values. Generally, this comparison would be mostly efficient away from the critical curves and cluster galaxies, where the magnification diverges or is highly perturbed. We use this information as a consistency check as shown in Figure 28 and in Table 1. For this purpose we use here the i'_{775} magnitudes, since it better constrains the magnitudes of higher-z galaxies. Other important aspects of the magnification map are the locations of the tangential and radial critical curves, were the latter to exist. The location of the tangential critical curve determines (for a certain source redshift) where highly-magnified and significantly stretched images would form. The location of the radial critical curve determines where and whether radial arcs, pointing towards the cluster centre, should form. The tangential and radial critical curves, laid on the colour cluster image are shown in Figure 21 (along with the multiply-lensed systems). Also, we

Table 1. Known and new multiple-images systems discovered by the model. For more detailed information on each system and other optional members please see the corresponding subsection. The columns are: arc ID; RA and DEC in J2000.0; the i'_{775} magnitude in the AB system; relative magnification - these values represent the lensing-model predicted magnitude difference, between the first image of each system and each of the following images, based on the relative magnifications (see §4.6.3); the lensing-model predicted redshifts; the photometric redshifts, as obtained from the highest peak photo-z distribution and errors. Note that some images were not covered by the NIC3 imaging and therefore their photo-z relies on ACS photometry alone. Note also that the errors are very large in cases where the photo-z distribution is bimodal (see images 6.1 and 9.3 in Figures 13 and 16, respectively). In such cases the values which agree with the SL model can be different than specified in this Table, as they arise from other peaks in the distribution, as detailed in the corresponding paragraphs; the χ^2 of the photometric redshift fitting procedure.

ARC ID	RA (J2000.0)	DEC (J2000.0)	i'_{775} (AB mag)	Relative magnification	z_{model}	z_{phot}	χ^2
1.1	00 26 34.43	17 09 55.4	21.333±0.008	—	—	1.44 ± 0.24	0.29
1.2	00 26 35.45	17 09 43.1	21.152±0.009	-0.229	"	0.60 ± 0.16	0.26
1.3	00 26 37.19	17 09 15.8	20.641±0.006	-0.207	"	1.45 ± 0.24	0.41
1.4	00 26 37.72	17 09 25.7	21.264±0.007	0.290	"	0.71 ± 0.17	0.68
1.5	00 26 37.99	17 09 41.2	20.988±0.007	-0.458	"	1.46 ± 0.24	0.39
2.1	00 26 35.57	17 09 08.8	24.572±0.034	—	1.22 ± 0.1	$0.85^{+0.41}_{-0.18}$	0.29
2.2	00 26 35.79	17 09 52.7	24.734±0.041	-0.467	"	$1.24^{+0.22}_{-0.31}$	0.17
2.3	00 26 35.82	17 09 49.0	—	—	"	—	—
3.1	00 26 36.86	17 09 24.3	25.142±0.039	—	$2.55^{+0.45}_{-0.2}$	$2.76^{+0.37}_{-2.59}$	2.60
3.2	00 26 35.66	17 10 18.4	25.176±0.039	-0.201	"	2.48 ± 0.34	0.15
3.3	00 26 34.74	17 10 12.6	25.953±0.071	0.200	"	$2.51^{+0.34}_{-2.19}$	0.26
3.4	00 26 32.92	17 09 46.6	25.070±0.040	-0.005	"	$2.58^{+0.35}_{-2.38}$	0.53
4.1	00 26 34.59	17 09 42.1	24.454±0.028	—	1.96 ± 0.20	$2.13^{+0.31}_{-0.33}$	0.15
4.2	00 26 34.75	17 09 41.5	24.608±0.036	0.242	"	$2.30^{+0.34}_{-0.68}$	0.20
4.3	00 26 38.73	17 09 38.6	26.088±0.060	0.403	"	$2.28^{+0.36}_{-2.07}$	0.74
5.1	00 26 32.86	17 09 39.3	26.168±0.083	—	2.02 ± 0.20	$0.25^{+2.44}_{-0.12}$	1.23
5.2	00 26 36.76	17 09 31.9	26.083±0.068	0.130	"	$1.58^{+0.65}_{-1.52}$	1.40
6.1	00 26 35.13	17 09 49.4	23.494±0.038	—	$1.93^{+0.15}_{-0.12}$	$0.38^{+3.23}_{-0.13}$	0.17
6.2	00 26 37.78	17 09 04.7	27.444±0.173	-0.159	"	$0.46^{+2.59}_{-0.18}$	1.44
7.1	00 26 35.58	17 10 05.9	25.587±0.158	—	$2.15^{+0.28}_{-0.26}$	$0.90^{+0.33}_{-0.38}$	1.05
7.2	00 26 36.22	17 09 03.0	25.137±0.116	-0.019	"	$1.23^{+0.22}_{-0.23}$	0.71
8.1	00 26 36.38	17 08 55.9	25.755±0.052	—	4.03 ± 0.5	4.09 ± 0.50	0.29
8.2	00 26 35.01	17 10 02.8	26.592±0.082	0.182	"	$4.16^{+0.51}_{-3.62}$	0.43
9.1	00 26 34.66	17 09 28.9	26.296±0.068	—	$1.96^{+0.5}_{-0.1}$	3.46 ± 0.44	0.83
9.2	00 26 34.67	17 09 29.2	26.211±0.064	-0.007	"	3.40 ± 0.43	0.81
9.3	00 26 37.53	17 10 06.8	26.568±0.076	0.033	"	$0.38^{+3.05}_{-0.17}$	0.81
10.1	00 26 36.17	17 09 42.3	24.703±0.034	—	$0.96^{+0.23}_{-0.20}$	0.75 ± 0.17	1.35
10.2	00 26 36.11	17 09 42.7	24.478±0.036	1.157	"	$0.58^{+0.16}_{-0.15}$	1.61
10.3	00 26 33.65	17 09 42.6	26.618±0.082	1.042	"	$0.85^{+0.31}_{-0.26}$	0.42
11.1	00 26 34.31	17 09 56.6	26.927±0.088	—	2.5 ± 0.5	$2.83^{+0.38}_{-2.67}$	0.25
11.2	00 26 37.34	17 09 08.6	24.773±0.033	-0.407	"	2.80 ± 0.37	0.06
11.3	00 26 38.05	17 09 18.1	25.326±0.042	0.026	"	$2.74^{+0.37}_{-2.49}$	1.01
11.4	00 26 38.45	17 09 37.8	26.025±0.058	-0.452	"	$3.22^{+0.41}_{-2.99}$	1.28

show in a separate Figure (22), the radial images around the radial critical curve. In addition, the magnification profiles of the best-fitting models are plotted in Figure 23 where we also plot the radii of the critical curves.

5.3 The Mass Profile and Comparison with Weak Lensing

The mass profiles of the acceptable best-fitting models (Figure 6) are very similar to each other within the errors, with a mean slope of $d\log M/d\log r \simeq -0.55\pm0.06$ (see also Figure 26). These profiles are effectively limited to a maximum radius of approximately $50''$, or ~ 250 kpc/h_{70}, corresponding to the outer limit of our multiply-lensed galaxies, which is

approximately twice the Einstein radius. The slope we measure is similar to that obtained by Broadhurst et al. (2005a) based on a 106 multiple images in A1689, and for A1703 (Saha & Read 2009, Figure 5) based on 42 images identified by Limousin et al. (2008).

In the very inner region we do not detect arcs at a radius below $\sim 5''$, setting an effective lower limit of $\simeq 27$ kpc/h_{70}. In defining a meaningful radial profile we must have a good idea of the centre of mass and also the effect of any substructure. We take as our preferred estimate of the centre of mass to be the centre of the inner radial critical curve which is found to be fairly circular. This centre is close, within $3''$, (16 kpc/h_{70}) but not coincident with the brightest cD galaxy. There is no reason to expect a coincidence between
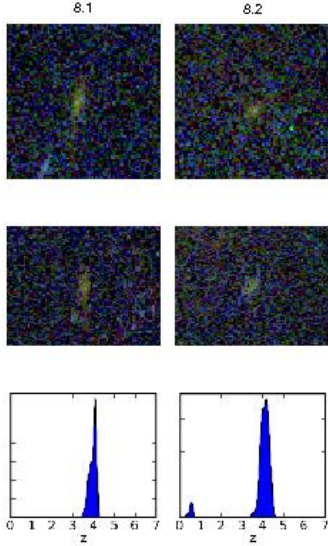
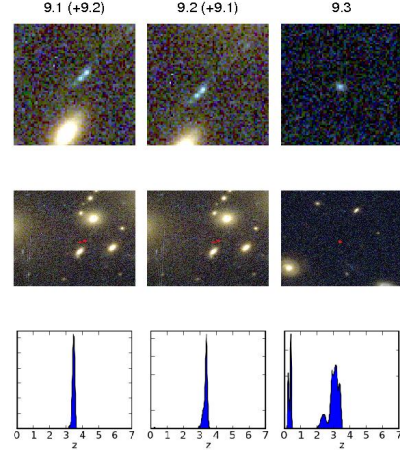**Figure 15.** System number 8: The two images of this system are shown in the top row, where below them we add the model-reproduced images on similar artificial background. The third row is the photo-z distributions of the images which agree with our $z \sim 4$ model prediction. Note that this system has the highest source redshift among the images found here as its images show the characteristic break expected from a distant drop-out galaxy, and it was used to strongly constrain the mass profile, as detailed in §4.7.

Figure 16. System number 9: The three images of this system are shown in the top row, where below them we add the model-reproduced images. The third row is the photo-z distributions of the images. Note that the photo-z of images 9.1 and 9.2 is badly affected by galaxy light, and we rely on the photo-z distribution of image 9.3, which agrees with our $z \sim 2$ model prediction. Images 9.1 and 9.2 are, as shown by our model, two different images, straddling the radial critical curve. Also, due to the vicinity of images 9.1 and 9.2 to a cluster member, the colour delensing-relensing procedure is seriously contaminated. We therefore lens each image of this system to reproduce its counter image, painted in red to emphasise the accuracy of the model with respect to the images location. This is seen in the second row, where we also zoom out in order to better show the relative location of the reproduced images in the cluster. Note that the orientation of the combined image 9.1+9.2 is slightly different than the original as it is strongly locally affected by the nearby cluster galaxy.

the centre of mass of a cluster and a cD galaxy, an object which presumably follows a complex inner orbit about a dynamically evolving centre of mass. In some cases significant velocity differences are found between the cD galaxy in a cluster and the systemic velocity of a cluster determined from many cluster members. A small but significant difference of this sort was also seen in the detailed mass map recovered for A1689 where many central images help to constrain well the mass distribution. SL models are often built with fewer multiple images and often the location of the cD galaxy is taken to be the projected centre of mass of the cluster for want of better data.

In 2D the mass distribution shows two small substructures containing less than $\sim 10\%$ of the total mass within the SL area. Overall the central mass distribution is fairly symmetric and centrally concentrated similar to the distribution of bright cluster members though not strictly in proportion, as discussed in section §4.2. We may compare this radial mass profile with that recently obtained from a new weak lensing analysis by Umetsu et al. (2009, in prep). This is based on deep multi-colour Subaru imaging in B'R'Z' and a two colour selection of red and blue background galaxies, similar to that employed by Medezinski et al. (2009, in prep) for a sample of other deeply-imaged clusters observed with Subaru. Good agreement is found between the SL mass profile and the WL as reconstructed from the WL measurements in the region where the profiles overlap, as shown in figure 26.

This agreement is very reassuring, particularly because the WL determination is model-independent. Also this demonstrates that there is no mismatch when systematic effects, in particular the selection of background galaxies, are properly dealt with. Dilution of the WL signal by cluster members and unlensed foreground galaxies has been identified as a longstanding widespread problem (Broadhurst et al. 2005b), responsible for the often much smaller Einstein radius predicted for models fitted to WL data than the observed Einstein radius.

If we fit an NFW model to the joint weak and strong lensing profile we obtain a reasonable fit with a concentration of $c_{\mathrm{vir}} = 8.6 \pm 1.6$ (Umetsu et al. 2009, in prep.). The inner profile is somewhat shallower than the canonical NFW profile best-fitting model to the overall data - and similar to that obtained for A1689 by Broadhurst et al. (2005a). A significant substructure is found in the WL maps at a radius of about $3.5'$ from the cluster centre, in good agreement with the location of a secondary sub-structure found by Kneib et al. (2003), based on independent mosaic HST imaging. The effect of this substructure, although modest, is significant in the derivation of the overall concentration and is treated in full detail by Umetsu et al. (2009, in prep.). Here we stress only the good empirical agreement between the
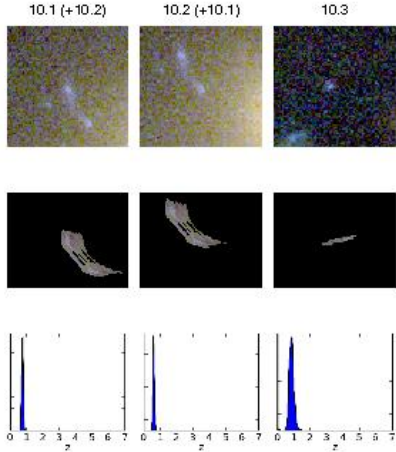
10.1 (+10.2)   10.2 (+10.1)   10.3

11.1   11.2   11.3   11.4

Figure 17. System number 10: The three images of this system are shown in the top row, where below them we add the model-reproduced images. The third row is the photo-z distributions of the images. Note that the photo-z of images 10.1 and 10.2 is badly affected by galaxy light, and we rely on the photo-z distribution of image 10.3, which agrees well with our $z \sim 1$ model prediction. Images 10.1 and 10.2 are radial images straddling the radial critical curve. Also, due to the vicinity of these images to cluster members, the colour delensing-relensing procedure is relatively noisy, but it is sufficient to show the relevant internal structure. Note that the relensed images are somewhat bigger, as some of the noise gets lensed as well.

Figure 18. System number 11: The four images of this system are shown in the top row, where below them we add the model-reproduced images on similar artificial background. The third row is the photo-z distributions of the images, which agree well with the our model $z \sim 2.5$ prediction. This system imitates the location of the main 5-image system, with a larger radius (and therefore redshift) comprising four blue images with internal bright spots, next to images 1.1, 1.3, 1.4 and 1.5, respectively, and well reproduced by our model. A very small image is predicted in the cluster centre near 1.2, but was not found, probably due to the bright member light and uncertain subtraction at the predicted location.

weak and strong lensing in the region of overlap which we take as independent support for our SL solution.

6   SUMMARY AND CONCLUSIONS

We have presented a simple and accurate strong-lensing model for the galaxy cluster Cl0024+1654, based on ACS/NIC3/GTO images. This modelling has identified many multiply-lensed systems, which in turn were incorporated into the model to improve the fit, mainly by the use of their photo-z measurements. We have found that for the purpose of identifying multiple images, a wide range of profile slopes can be tolerated. This is an inherent lensing degeneracy that can be made use of, in the sense that those parameters controlling the overall profile slope can be initially set to reasonable values, enabling detection of multiply-lensed systems using only 4 free parameters, which are fully constrained by known systems. However, the model-predicted redshift for each system is sensitive to the profile slope and so we have made use of our relatively accurately-determined photo-z measurements to constrain the slope by minimising the parameters controlling the profile slope with respect to the standard cosmological distance-redshift relation.

The presented SL modelling-method uses only 6 free parameters, which is significantly less than other competing methods, in particular the model-independent approaches where the lens plane is described by a set of large pixels
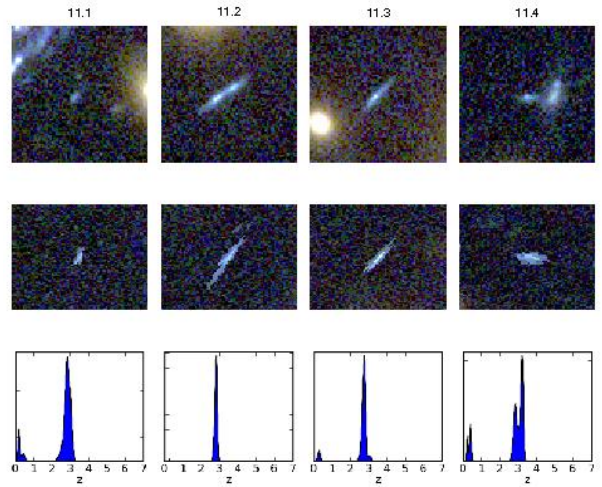
or with orthogonal functions etc. One relative disadvantage of our method is manifested in the reproduction accuracy of the multiply-lensed systems, with respect to the image-plane RMS and internal shape. For example, here the image-plane RMS is typically $\sim 2.5''$ *per image*, whereas Broadhurst et al. (2005a) achieved an RMS of $3.2''$ per image for A1689, and later Halkola, Seitz, & Pannella (2006) reported an RMS of $2.7''$ per image for that cluster. Quantifying these results relative to the size of the Einstein radius, Broadhurst et al. (2005a) and Halkola, Seitz, & Pannella (2006) obtained a $\sim$20% better image-plane RMS than achieved here. Naturally, a higher number of parameters would supply a more accurate solution, however, the efficiency of a model decreases extremely rapidly as more parameters are added to the minimisation procedure, and the confidence in the model decreases as more arbitrary non-physical parameters are added, as is often the case in other methods. We have shown that the presented method, with only 6 free parameters built on simple physical considerations, does a very good job in finding new multiply-lensed systems and in constraining the deflection field and accordingly the mass distribution and profile.

A smooth low-order fit is found to be a good representation of the overall mass distribution of the cluster, with a small contribution required from the observed cluster member galaxies. With this model we have accurately reproduced the well known 5-image system in this cluster field, and
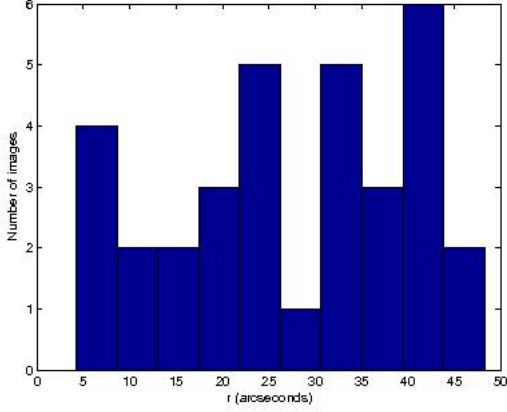
Figure 19. Radial distances from the cluster centre of all multiply-lensed images.
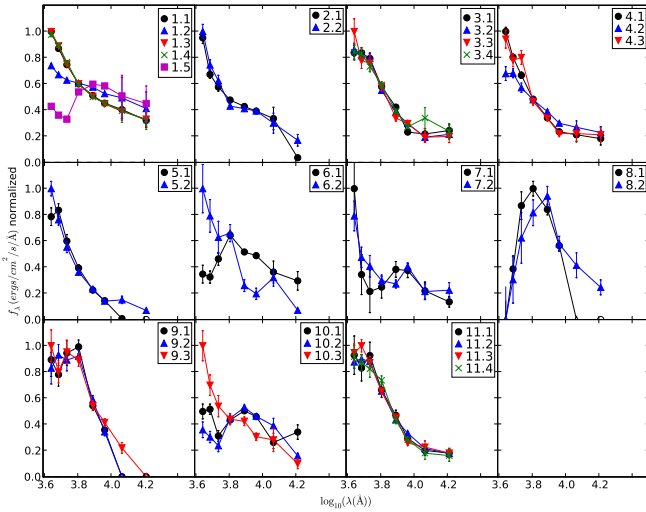

Figure 20. SED comparison of multiple image candidates of each lensed galaxy. We plot $BVg'r'i'z'JH$ photometry from ACS and NIC3 images. Good agreement is expected unless the light is contaminated by neighbouring galaxies. We identify these cases by visual examination of the images.

confirmed the tentative 2 image system identified in earlier WFPC-2 based modelling (Broadhurst et al. 2000), finding an additional third image associated with this source. In addition we identify 9 other multiple-images systems, bringing the total known for this cluster to 33 multiply-lensed images, spread fairly evenly all over the central area, $r \leqslant 50''$. We stress that our multiple images are accurately reproduced by our model and not simply eyeball candidates requiring redshift verification.

Our best fitting model minimises the image-plane RMS of the reconstructed image location compared with the observed positions. We also find this model satisfies three other completely independent criteria. Firstly the best fit solution recovers the expected cosmological relation of d_{ls}/d_s versus redshift for all sources with reliable photometric redshifts.
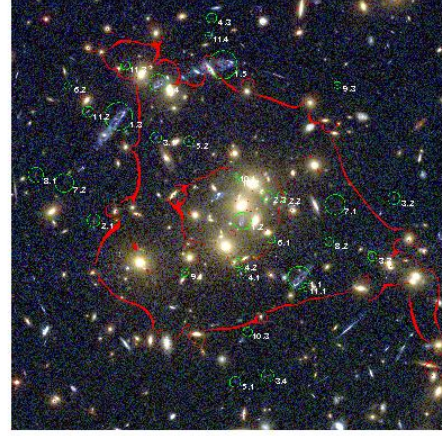
Figure 21. Magnification map (of a source at $z = 1.675$) laid over ACS colour-combined image, along with the multiply-lensed images marked in green. North is right, east is up. The field of view is $\sim 100'' \times 100''$.
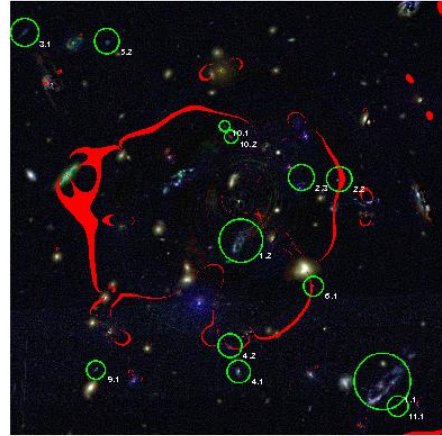
Figure 22. A galaxy subtracted image, zoomed-in on the radial critical curve and the images defining it. The radial curve in the image is for a source at $z = 1.675$. North is right, east is up. The field of view is $\sim 40'' \times 40''$.

We also find that the predicted and derived relative magnifications of the multiple images are also well reproduced (see Figure 28). In addition, we find good agreement between our SL-based mass profile and the mass profile recovered from WL in the region of overlap of these profiles, implying an NFW profile with a concentration of $c_{\mathrm{vir}} = 8.6 \pm 1.6$. These independent consistency checks reassure us that the derived mass distribution is a reliable representation of the central mass distribution. The success of this simple and minimalistic method we have applied here motivates an analysis of larger statistical well-defined samples of massive relaxed
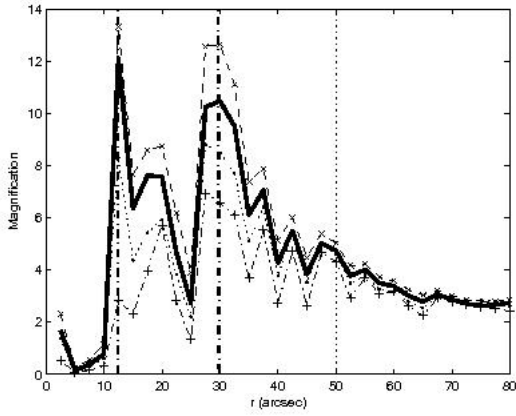
Figure 23. The resulting magnification profile. The solid thick line is the best model magnification-profile, where the errors are represented by the dashed lines denoted as in Figure 6. The dashed vertical lines are the radial and tangential critical radii (as determined by eye), and the 50″ line which indicates the range within which multiple images were found.
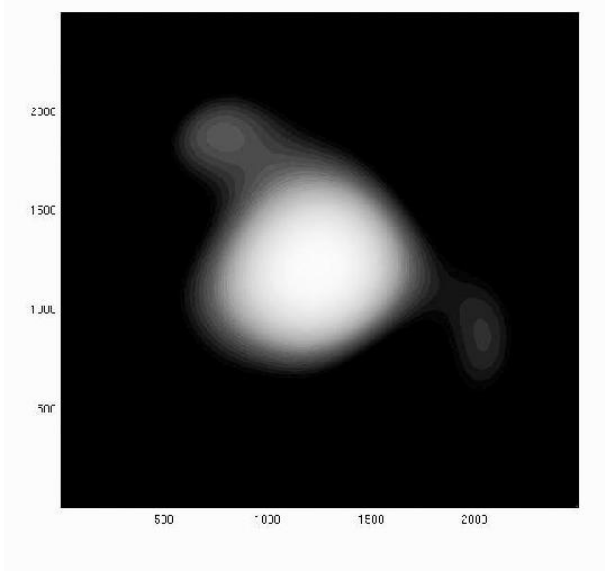

Figure 25. The total (galaxies+DM) final mass distribution. North is right, east is up. Axes are in pixels.

Figure 24. The resulting smooth DM distribution. Note that it is fairly circular with two small clumps. North is right, east is up. Axes are in pixels (where the pixel scale is 0.05 ″/pixel).
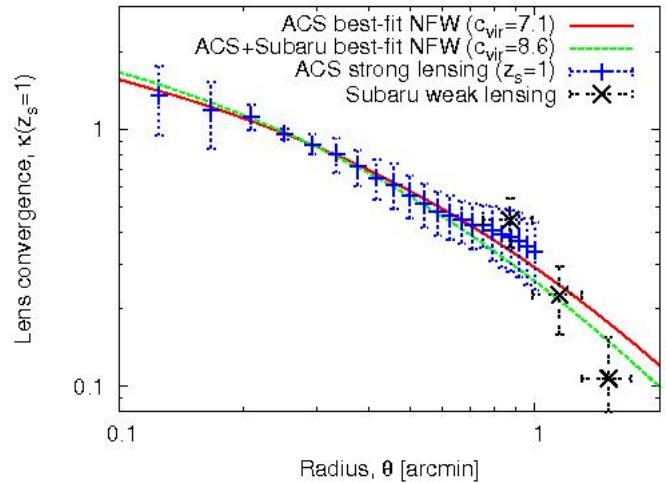
Figure 26. Comparison of weak and strong lensing determinations of surface mass densities. Good consistency is found here between these very different, independent measurements. The best fitting NFW profile is indicated, for SL alone (red), and in combination with WL (green), see Umetsu et al. (2009, in perp).

clusters, which should be helpful in constraining in a new way the cosmological curvature, and shed more light on the nature of DM by comparison with the increasingly accurate predictions for the properties of DM dominating massive galaxy clusters.
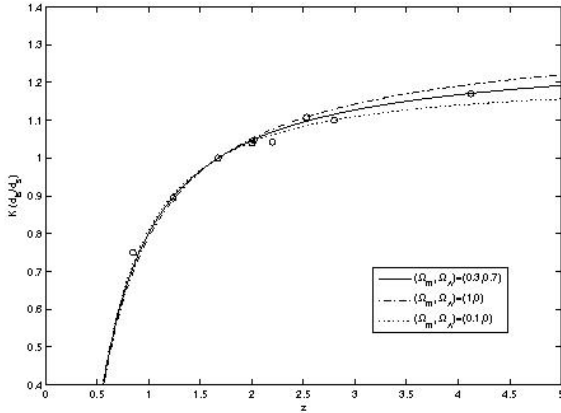
Figure 27. Growth of the scaling factor K_q as a function of redshift, normalised so $K_q=1$ at $z=1.675$. Plotted lines are the expected ratio from the chosen specified cosmology. The points are the multiple-image systems. The data follow very well the relation predicted by the standard cosmology.
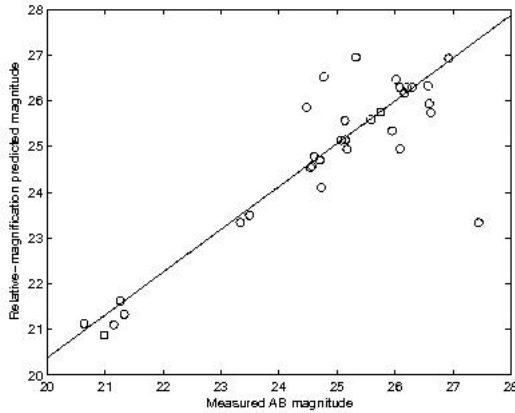

Figure 28. Relation between the measured AB magnitudes and the model-predicted magnitudes, as derived from the relative magnifications as explained in §4.6.3. As can be seen, these are closely proportional.

REFERENCES

Abdelsalam, H. M., Saha, P., & Williams, L.L.R., 1998, AJ, 116, 1541

Ascaso, B., et al., in prep.

Benítez, N., 2000, ApJ, 536, 571

Benítez, N., et al., 2004, ApJS, 150, 1

Bertin, E. & Arnouts, S., 1996, A&AS, 117, 393

Blakeslee, J. P., Anderson, K. R., Meurer, G. R., Benítez, N., Magee, D., 2003, in Astronomical Society of the Pacific Conference Series, Vol. 295, Astronomical Data Analysis Software and Systems XII, ed. H. E. Payne, 257

Blumenthal, G.R., Faber, S.M., Flores, R., Primack, J.R., 1986, ApJ, 301, 27y

Bouwens, R.J., Illingworth, G.D., Bradley, L.D., Ford, H., Franx, M., Zheng, W., Broadhurst, T., Coe, D., Jee, M. J., 2008, arXiv0805.0593

Bradley, L. D., et al., 2008, ApJ, 678, 647

Broadhurst, T., Huang, X., Frye, B., Ellis, R., 2000, ApJ, 534, L15

Broadhurst, T., et al. 2005a, ApJ, 621, 53

Broadhurst, T., Takada, M., Umetsu, K., Kong, X., Arimoto, N., Chiba, M., Futamase, T., 2005b, ApJ, 619, 143

Broadhurst, T. & Barkana, R., 2008, MNRAS, 390, 1647

Broadhurst, T., Umetsu, K., Medezinski, E., Oguri, M., Rephaeli, Y., 2008, ApJ, 685, 9

Bullock, J.S., Kolatt, T.S., Sigad, Y., Somerville, R.S., Kravtsov, A.V., Klypin, A.A., Primack, J.R., Dekel, A. 2001, MNRAS, 321, 559

Clowe, D. & Schneider, P., 2001, A&A, 379, 384

Coe, D., Benítez, N., Sánchez, S. F., Jee, M., Bouwens, R., Ford, H., 2006, AJ, 132, 926

Coe, D., Fuselier, E., Benítez, N., Broadhurst, T., Frye, B., Ford, H., 2008, ApJ, 681, 814

Colley, W. N., Tyson, J.A., & Turner, E.L., 1996, ApJ, 461, L83

Corless, V.L., King, L.J., Clowe, D., 2008, arXiv0812.0632

Diego, J.M., Sandvik, H.B., Protopapas, P., Tegmark, M., Benítez, N., Broadhurst, T., 2005, MNRAS,362, 1247

Duffy, A.R., Schaye, J., Kay, S.T., & Dalla Vecchia, C. 2008, MNRAS, 390, 64

Franx, M., Illingworth, G. D., Kelson, D. D., van Dokkum, P. G., & Tran, K. 1997, ApJ, 486, L75

Frye, B. & Broadhurst, T., 1998, ApJ, 499, L115

Frye, B., Broadhurst, T., & Benítez, N., 2002, ApJ, 568, 558

Gavazzi, R., Fort, B., Mellier, Y., Pelló, R., Dantel-Fort, M., 2003, A&A, 403, 11

Halkola, A., Seitz, S., & Pannella, M., 2006, MNRAS, 372, 1425

Hennawi J.F., Dalal N., Bode P., Ostriker J.P., 2007, ApJ, 654, 714

Inada, N., et al., 2005, PASJ, 57, 7

Jee M.J., et al., 2007, ApJ, 661, 728

Kassiola, A., Kovner, I., & Blandford, R.D., 1992, ApJ, 396, 10

Keeton, C.R., Kochanek, C.S., & Seljak, U., 1997, ApJ, 482, 604

Kneib, J.-P., Hudelot, P., Ellis, R.S., Treu, T., Smith, G.P., Marshall, P., Czoske, O., Smail, I., Natarajan, P., 2003, ApJ, 598, 804

Kneib, J.-P., Ellis, R.S., Santos, M.R., Richard, J., 2004, ApJ, 607, 697

Koo, D.C., 1988, in Large-Scale Motions in the Universe, ed. V.G. Rubin & G.V. Cayne (Princeton: Princeton Univ.Press), 513

Kovner, I., 1987a, ApJ, 312, 22

Kovner, I., 1987b, ApJ, 316, 52

Lemze, D., Barkana, R., Broadhurst, T., Rephaeli, Y., 2008a, MNRAS, 386, 1092

Lemze, D., Broadhurst, T., Rephaeli, Y., Barkana, R., Umetsu, K., 2008b, arXiv0810.3129

Liesenborgs, J., de Rijcke, S., Dejonghe, H., Bekaert, P., 2008a, MNRAS, 386, 307

Liesenborgs, J., de Rijcke, S., Dejonghe, H., Bekaert, P., 2008b, MNRAS, 389, 415

Limousin, M., 2008, A&A, 489, 23

Magee, D.K., Bouwens, R.J. & Illingworth, G.D. 2007, Astronomical Data Analysis Software and Systems XVI, ASP Conference Series, eds. R.A. Shaw, F. Hill, & D.J. Bell, (ASP: San Francisco), 376, 261

Medezinski, E., Broadhurst, T., Umetsu, K., Coe, D., Benítez, N., Ford, H., Rephaeli, Y., Arimoto, N., Kong, X., 2007, ApJ, 663, 717

Medezinski, E., et al., 2009, in prep

Navarro, J.F., Frenk, C.S., & White, S.D.M., 1997, ApJ, 490, 493 (NFW)

Narayan, R. & Bartelmann, M., Lectures on Gravitational Lensing, 1996, arXiv:astro-ph/9606001v2

Neto, A.F., et al., 2007, MNRAS , 381, 1450

Oguri, M., et al., 2004, ApJ, 605, 78

Oguri, M., Takada, M., Umetsu, K., Broadhurst, T., 2005, ApJ, 632, 841

Oguri, M., Hennawi, J.F., Gladders, M.D., Dahle, H., Natarajan, P., Dalal, N., Koester, B.P., Sharon, K., Bayliss, M., 2009, arXiv0901.4372O

Sadeh, S. & Rephaeli, Y., 2008, MNRAS, 388, 1759

Saha, P. & Read, J.I., 2009, ApJ, 690, 154

Sharon, K., Ofek, E.O., Smith, G.P., Broadhurst, T., Maoz, D., Kochanek, C.S., Oguri, M., Suto, Y., Inada, N., Falco, E.E., 2005, ApJ, 629, 73

Smail, I., Dressler, A., Kneib, J.-P., Ellis, R.S., Couch W.J., Sharples, R.M., Oemler, A., 1996, ApJ, 469, 508

Spergel, D.N., et al., 2003, ApJS, 148, 175

Spergel D.N., et al., 2007, ApJS, 170, 377

Springel et al., 2005, Nature, 435, 629

Stark, D.P., Ellis, R.S., Richard, J., Kneib, J.-P., Smith, G.P., Santos, M.R., 2007, ApJ, 663, 10

Tegmark, M., et al., 2004, ApJ, 606, 702

Tyson, J.A., Kochanski, G.P., & dell'Antonio, I.P., 1998, ApJ, 498, L107

Umetsu, K. & Broadhurst, T., 2008, ApJ, 684, 177

Umetsu, K., et al., 2009, in prep.

Wallington, S., Kochanek, C.S., & Koo, D.C., 1995, ApJ, 441, 58

Zheng, W., et al., 2009, in prep.

Zwicky, F., 1959, Handbuch Phys., 53, 390

This paper has been typeset from a TEX/ LATEX file prepared by the author.